



CHALMERS
UNIVERSITY OF TECHNOLOGY

Tuning the ground state of cuprate superconducting thin films by nanofaceted substrates

Downloaded from: <https://research.chalmers.se>, 2024-08-17 03:20 UTC

Citation for the original published paper (version of record):

Mirarchi, G., Arpaia, R., Wahlberg, E. et al (2024). Tuning the ground state of cuprate superconducting thin films by nanofaceted substrates. *Communications Materials*, 5(1).
<http://dx.doi.org/10.1038/s43246-024-00582-5>

N.B. When citing this work, cite the original published paper.

<https://doi.org/10.1038/s43246-024-00582-5>

Tuning the ground state of cuprate superconducting thin films by nanofaceted substrates



Giovanni Mirarchi¹, Riccardo Arpaia ^{2,3}, Eric Wahlberg ^{2,4}, Thilo Bauch², Alexei Kalaboukhov², Sergio Caprara¹, Carlo Di Castro¹, Marco Grilli ¹, Floriana Lombardi ²✉ & Götz Seibold ⁵✉

Anisotropic transport properties have been assessed in a number of cuprate superconductors, providing evidence for a nematic state. We have recently shown that in ultra-thin $\text{YBa}_2\text{Cu}_3\text{O}_{7-\delta}$ films, where nematicity is induced via strain engineering, there is a suppression of charge density wave scattering along the orthorhombic a -axis and a concomitant enhancement of strange metal behavior along the b -axis. Here we develop a microscopic model, that is based on the strong interaction between the substrate facets and the thin film, to account for the unconventional phenomenology. Based on the atomic force microscopy imaging of the substrates' surface, the model is able to predict the absence (presence) of nematicity and the resulting transport properties in films grown on SrTiO_3 (MgO) substrates. Our result paves the way to new tuning capabilities of the ground state of high-temperature superconductors by substrate engineering.

The ground state of cuprate high-critical-temperature superconductors (HTS) exhibits a fascinating interplay of quantum phases, where charge, spin and orbital orders are intertwined^{1–4}. Superconductivity emerges from a metallic state, named “strange metal”⁵, with properties that cannot be accounted for by the Fermi liquid theory. In this state, the quasiparticle picture breaks down and a robust T -linear dependence of the resistivity is observed, as if the details of the scattering events become irrelevant in a certain temperature range^{6–10}.

Modeling the strange metal state is challenging due to the strong electron-electron interactions. Recent work has addressed the problem of T -linear resistivity within advanced computational methods applied to the two-dimensional Hubbard model^{11,12}. Other approaches, involving critical fluctuations in the vicinity of a quantum critical point^{13–16}, e.g., based on short ranged dynamical charge density fluctuations^{17,18}, were also able to reproduce the fingerprint of this state of matter^{19,20}. Holographic duality, which maps the physics of strongly interacting systems onto the classical theory of gravity in higher dimensions, is a further pathway to obtain the T -linear resistivity^{21,22}.

Though encouraging, these theoretical attempts require further developments. The tuning of the ground state of HTS beyond oxygen doping, demonstrated in recent mechanical strain experiments^{23–31}, can give additional information about the strange metal phase, its origin and the

intertwining with the various local orders, including charge density waves (CDW)^{32–37}. These new inputs could be fed into theories to discriminate between different scenarios.

In a recent experiment³⁸, where we studied the transport properties of ultrathin films as a function of doping, we have shown that the substrate-induced strain strongly modifies the ground state of the material affecting the Fermi surface topology, the strange metal phase and the CDW order. It is therefore natural to ask what the role of strain is in nm-thick films. Is it just the strain-induced geometrical modification of the unit cell that is important or does the substrate-film interface coupling induce subtler effects, possibly intertwined with other orders?

To answer these questions, we compare the resistivity measurements of 10 nm thick $\text{YBa}_2\text{Cu}_3\text{O}_{7-\delta}$ (YBCO) films grown on (110) MgO and (001) SrTiO_3 (STO) substrates, extensively studied in ref. 38, having different lattice parameters and surface morphologies. Using as input the experimental data from atomic force microscopy (AFM), we develop a model which describes different film-substrate coupling, depending on the extension and morphology of the surface facets. The results can nicely reproduce the nematic Fermi surface in the case of MgO, while confirming an unaltered ground state with STO. Starting from a nematic Fermi surface we retrieve the unidirectional CDW observed in the experiment³⁸ and discuss the possible implication on the strange metal state.

¹Dipartimento di Fisica, Università di Roma ‘La Sapienza’, Roma, Italy. ²Quantum Device Physics Laboratory, Department of Microtechnology and Nanoscience, Chalmers University of Technology, Göteborg, Sweden. ³Department of Molecular Sciences and Nanosystems, Ca’ Foscari University of Venice, Venice, Italy.

⁴RISE Research Institutes of Sweden, Borås, Sweden. ⁵Institut für Physik, BTU Cottbus-Senftenberg, Cottbus, Germany.

✉ e-mail: floriana.lombardi@chalmers.se; goetz.seibold@b-tu.de

Figure 1 summarizes the transport properties at $p = 0.12$ of our 10 nm thick YBCO films, on both MgO and STO, as we have shown in ref. 38. Here, the doping level has been calibrated through measurements of the c -axis length and of the critical temperature, according to the procedure extensively discussed in ref. 39. Figure 1a shows the temperature dependence of the resistivity ρ , measured in two devices oriented along the YBCO a - and b -axis, realized in an untwinned film grown on MgO. The anisotropy ratio at $T = 290$ K, defined by $\rho_a(290 \text{ K})/\rho_b(290 \text{ K})$, exceeds 2, a value much higher than that measured in our thicker YBCO films, cf. Supplementary Note 4. The slopes of $\rho_a(T)$ and $\rho_b(T)$ are quite different, indicating different Fermi velocities along a - and b -axis, and thus a nematic Fermi surface³⁸. In these samples, both the strange metal state and the CDW become very anisotropic. The T -linear behavior along b is extended down to $T_L = 187$ K, while along a T_L is the same as in bulk samples. Simultaneously, the CDW measured by resonant inelastic X-ray scattering (RIXS) becomes unidirectional along b ³⁸. These anisotropies are doping dependent, being observed only within the range $0.11 \lesssim p \lesssim 0.16$; for $p < 0.11$, the typical isotropic behavior seen in bulk samples, e.g., $T_L^a = T_L^b$, is restored³⁸.

In underdoped, untwinned, 10 nm thick YBCO films grown on (001) STO substrates with a vicinal angle, the transport properties along a - and b -axis are more conventional and resemble bulk samples. Here, at $p = 0.12$, the slopes of the T -linear resistivity are very similar for $\rho_a(T)$ and $\rho_b(T)$ [see Fig. 1b], indicating comparable Fermi velocities along both axes and therefore a rather isotropic Fermi surface. Moreover, the strange metal state and the CDW exhibit no anisotropy, unlike the MgO case³⁸.

The large difference in transport properties between films grown on MgO and on STO, despite the identical doping levels, suggests that the nematicity, conspicuous only in films grown on MgO, cannot be solely attributed to the CuO chains along the b -axis, since these are present and equally filled in both systems. To shed light on this peculiar anisotropic state, we investigated the substrate surface structure and its interface with the YBCO films.

The surface of (110) oriented MgO substrates exhibits elongated nanofacets, running along the [001] direction. They are due to surface reconstruction, achieved through substrate annealing, which is instrumental to get untwinned YBCO films⁴⁰. Tapping mode (TM) AFM investigation demonstrates that these nanofacets have an average height of about 1.5 nm

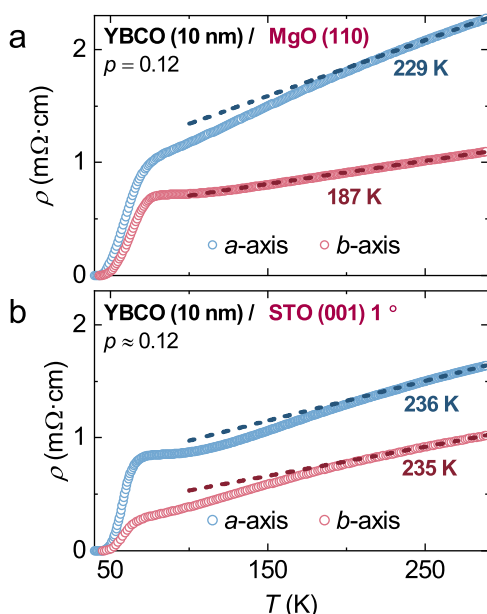


Fig. 1 | Strain dependence of the in-plane resistivity of underdoped YBCO films (thickness $t = 10$ nm). **a** $\rho(T)$ along the a - and b -axis of a film grown on MgO. The dashed lines are the linear fits of the curves for $T > 260$ K. Close to these lines, the temperatures below which the resistivity deviates by 1% from the linear behaviour are reported. **b** Same as **a**, but for a film grown on a 1° vicinal angle STO.

and a nearly triangular profile [see Fig. 2(a-c)]. This results in a very anisotropic atomic lattice, where large areas along the facet edges consist of under-coordinated atoms. This picture is confirmed by peak force quantitative nanomechanics (PFQNM) AFM adhesion analysis [see Fig. 2(a)], where the chemical contrast at the surface of the MgO substrate can be investigated. The difference in coordination between the atoms in the valleys and along the facet edges is very large, and affects a substantial area of the substrate surface. When YBCO is deposited on top of this surface [see the scanning electron microscopy image in Fig. 2(a)], it is subject to a very anisotropic strain, resulting in an untwinned film, with the a -axis and the b -axis respectively aligned perpendicular and parallel to the MgO facets⁴⁰. At the interface, the film is embedded in this articulated and anisotropic substrate matrix, with its unit cell height comparable to the nanofacet height. It is then natural to expect a strong film-substrate coupling, mainly occurring in the areas where the substrate atoms are under-coordinated. This strong coupling is based on the hybridization between the two layers to saturate these bonds and therefore only affects few YBCO layers adjacent to the substrate. It is thus particularly relevant for the transport properties of the 10 nm films analyzed in this paper.

Results and Discussion

Effective model for the coupling between thin film and substrate

Our model for this heterogeneous structure is depicted in Fig. 2 where the YBCO layer is represented by the red-dot lattice. The chemical coupling between CuO₂ plane and MgO substrate is described by a hopping t_\perp to the elongated regions of the substrate having under-coordinated atoms. Consequently, only the elongated (actually 1D) regions of the CuO₂ lattice along the b -axis are endowed by this additional t_\perp . The virtual hopping of charge carriers to the substrate atoms induces an effective repulsion between the

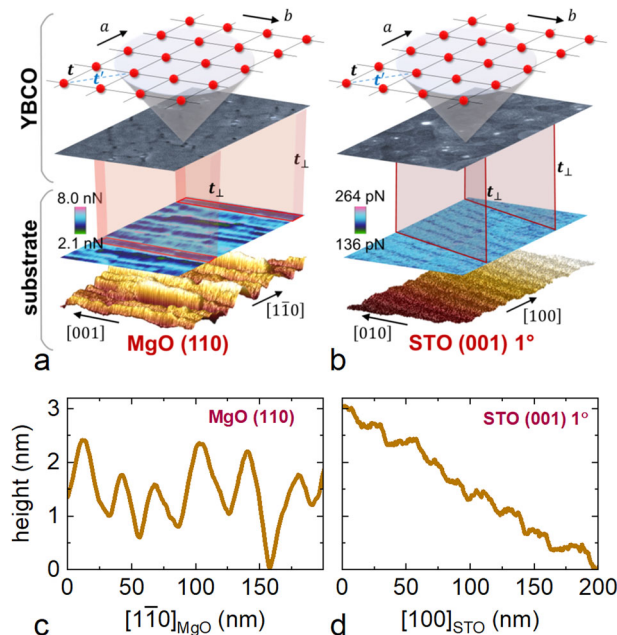


Fig. 2 | Analysis of the substrate surface and modeling of the interface with the YBCO film. **a** From the bottom: TM AFM image of a 250×250 nm² region of the annealed MgO (yellow-brown map). The chemical contrast caused by the elongated and rather high nanofacets is detected in the very same area by PFQNM AFM adhesion image (bluish map). The YBCO film grown on top is represented by a scanning electron microscopy image. The planar tight-binding structure of the YBCO planes is the topmost enlargement at the interatomic scale (red dots) with the nearest neighbor hopping parameter t and the next nearest neighbor hopping parameter t' . These atoms are those coupled to the under-coordinated regions of the substrate by a coupling parameter t_\perp (see the wide red slabs). **b** Same as **a**, but for a film grown on STO. **c** TM AFM linescan along the $[1\bar{1}0]$ MgO direction. **d** Same as **c**, but along the $[100]$ STO direction.

atomic levels of film and substrate, leading to an effective potential $V_{\text{eff}} = \frac{1}{2}(\sqrt{V_{\text{sub}}^2 + 4t_{\perp}^2} - V_{\text{sub}})$ for the coupled film atoms, where V_{sub} is the on-site energy of the coupled substrate atoms. The strips of atoms with the added t_{\perp} hopping are randomly distributed on the lattice, and can therefore be treated by a standard coherent potential approximation (CPA), see Supplementary Note 1.

For the YBCO/STO system, the 1° vicinality of the substrate results in step edges, having an average height of 3.9 \AA [STO lattice parameter, see Fig. 2(b-d)]. These steps induce an anisotropic strain, favoring the growth of untwinned YBCO films with the b -axis (a -axis) parallel (perpendicular) to the elongated steps. An effective, but much weaker, potential V_{eff} can again be used to describe the film-substrate coupling. Indeed, the atomic-scale-high steps of the STO substrates result in a tiny chemical contrast [see Fig. 2(b)], involving much narrower areas of the substrate surface (they are much sharper and reduced in height compared to the smooth slopes of the MgO nanofacets). In our model, the main difference between the two substrates is therefore given by the substantial different values of V_{eff} : $|V_{\text{eff}}| \sim t$, i.e., is of the order of the in-plane hopping t in case of MgO, playing a significant role in building up the YBCO electronic structure; for the STO substrate, instead, $|V_{\text{eff}}| \ll t$.

The model hamiltonian reads

$$H = \sum_{ij,\sigma} t_{ij} c_{i,\sigma}^\dagger c_{j,\sigma} + V_{\text{eff}} \sum_n \sum_{iy=1}^L c_{\mathbf{R}_n+iy\mathbf{b}}^\dagger c_{\mathbf{R}_n+iy\mathbf{b}} \quad (1)$$

where, t_{ij} includes hopping processes between nearest ($\sim t$) and next-nearest ($\sim tr$) neighbors, V_{eff} is the effective potential along the b -oriented strips with length L starting at a random site \mathbf{R}_n and the sum over these random sites is denoted by the primed sum. Given the large anisotropy of nanofacets and steps we further set $L \rightarrow \infty$ and encode the fraction of regions affected by the nanofacets or steps (the red slabs in Fig. 2) by the parameter f . In Eq. (1) f corresponds therefore to the fraction of sites on which the potential V_{eff} acts, i.e. $f = 1/N \sum_{iy=1}^L$ where N denotes the total number of sites. In the Supplementary Note 1 we also show that the modulation of the hopping in Eq. (1) can be neglected.

Owing to the random character of the strips and the expected smooth variation of the effective potential on atomic scales, we use a standard CPA (see Supplementary Note 1 for additional details). This allows to compute the self-energy and hence determine the Fermi surface for this disordered system. Figure 3 shows the Fermi surfaces, as obtained from an intensity plot of the momentum dependent spectral function at the Fermi energy, that result upon varying V_{eff}/t while keeping $f = 0.15$ constant. For small $V_{\text{eff}}/t = 0.2$ the Fermi surface [see Fig. 3(b)] remains unchanged from the unperturbed one [see Fig. 3(a)] and preserves the C_4 symmetry. Instead, when V_{eff}/t becomes significant, i.e., of the order as the in-plane hopping t (as in films on MgO), the Fermi surface becomes nematic, i.e., anisotropic and distorted in the regions around the points $(0, \pi)$ and $(\pi, 0)$ of the first Brillouin zone [see Fig. 3(c)]. This resembles the Fermi surface inferred in ref. 38 to explain the in-plane transport anisotropy observed in ultrathin YBCO films on MgO [see Fig. 1(a)].

CDW instabilities in the anisotropic effective model

This nematic Fermi surface has strong implications for the symmetry of the resulting charge collective excitations, which can affect the anisotropic transport properties of the films. In the following, we demonstrate that the Fermi surface in Fig. 3c, resulting from the anisotropy imposed by the MgO nanofacets, leads to a unidirectional CDW along the b -axis, consistent with observations in underdoped ($p = 0.12$) 10 nm thick YBCO films grown on MgO³⁸. To this purpose we adopt the framework of frustrated phase separation, where the charge instability is not driven by nesting properties of the Fermi surface, but merely results from the electron-electron Coulombic repulsion frustrating the phase separation induced by a variety of attractive mechanisms on a strongly correlated electron system^{41–45}.

This theory does not rely on strong coupling between spin and charge degrees of freedom, unlike the stripe phase of 214 cuprates. Hence, it provides an appropriate starting point for describing CDW in YBCO (as well as Bi- and Hg-based cuprates, where the magnitude of the CDW wave vector q_{CDW} decreases with doping). A minimal model for this scenario is given by^{43–46}

$$H = \sum_{\mathbf{k},\sigma} \epsilon_{\mathbf{k}} f_{\mathbf{k},\sigma}^\dagger f_{\mathbf{k},\sigma} - \frac{g}{\sqrt{N}} \sum_{\mathbf{q}} (a_{\mathbf{q}} + a_{-\mathbf{q}}^\dagger) \rho_{\mathbf{q}} + \omega_0 \sum_{\mathbf{q}} a_{\mathbf{q}}^\dagger a_{\mathbf{q}} + \frac{1}{2N} \sum_{\mathbf{q}} [V_{\text{coul}}(\mathbf{q}) + V_{\text{res}}(\mathbf{q})] \rho_{\mathbf{q}} \rho_{-\mathbf{q}} \quad (2)$$

where operators $f_{\mathbf{k}}^{(\dagger)}$ annihilate (create) quasiparticles that correspond to the low-energy sector of a strongly correlated ($U \rightarrow \infty$) model. The dispersion $\epsilon_{\mathbf{k}}$ contains the nematicity via a parametrization of the nearest-neighbor hopping $t_{b,a} = t(1 \pm \alpha)$ [see Fig. 3c], $\rho_{\mathbf{q}} = \sum_{\mathbf{k},\sigma} f_{\mathbf{k}+\mathbf{q},\sigma}^\dagger f_{\mathbf{k},\sigma}$ is the density operator in momentum space and N denotes the number of lattice sites. The hamiltonian Eq. (2) includes a coupling ($\sim g$) to a dispersionless phonon (frequency ω_0) which yields an effective attractive interaction between quasiparticles $-\lambda \equiv -g^2/\omega_0$. The latter is counteracted by a long-range Coulomb repulsion V_{coul} and a residual repulsion between quasiparticles $V_{\text{res}}(\mathbf{q})$ as it customarily occurs in Landau Fermi liquids.

In a Fermi liquid only subject to a constant (in momentum space) attractive interaction $V_{\text{tot}}(\mathbf{q}) = -\lambda$, a CDW transition occurs when the random-phase-approximation (RPA) condition $1/\chi_{pp}^0(\mathbf{q}) - V_{\text{tot}}(\mathbf{q}) = 0$ is satisfied. Here, $\chi_{pp}^0(\mathbf{q})$ is the charge susceptibility of the non-interacting quasiparticle system. Therefore, this instability occurs at the dominant nesting wave vector, i.e., where the charge susceptibility is maximum (kink in the black curve of Fig. 4). However, in a strongly correlated system, the electron dynamics can be mapped onto an effective low energy hamiltonian^{43–46}, see Eq. (2), where, according to the Fermi liquid paradigm, the large Hubbard repulsion U among electrons is turned into a residual repulsion between quasiparticles, $V_{\text{res}}(\mathbf{q})$ (red curve in Fig. 4), which is maximum at large wave vectors (short distances). Together with an attractive contribution $-\lambda$, the total interaction is minimum (and negative) at small momenta, satisfying the RPA criterion in general at $\mathbf{q} = 0$, corresponding to a phase separation instability. On the other hand, the long-range Coulomb repulsion $V_{\text{coul}}(\mathbf{q})$ (green curve in Fig. 4) spoils the zero-momentum charge instability, shifting \mathbf{q}_{CDW} to finite and in general incommensurate values. In a nematic system, all these contributions, determining the CDW instability, acquire an anisotropic character (analyzed in detail in the Supplementary Note 3). As specified in Eq. (2), we consider an attractive contribution solely due to a momentum independent ‘Holstein-type’ electron-phonon interaction $V^{\text{ph}}(\mathbf{q}) \equiv -\lambda$. This parameter must overcome a critical value (orange dashed arrow in Fig. 4) to trigger the CDW instability.

Over the whole doping range the nematic Fermi surface leads to an enhanced charge susceptibility $\chi_{pp}^0(\mathbf{q})$ along the b -axis. Three distinct doping regimes can be identified:

- At low doping, due to the effect of strong correlations, the residual repulsion $V_{\text{res}} \sim 1/p$ dominates the anisotropy of $V_{\text{tot}}(\mathbf{q})$, cf. Supplementary Note 3. Within a standard slave-boson approach^{46,47}, which is also outlined in the Supplementary Note 2, $V_{\text{res}}(\mathbf{q})$ is proportional to the quasiparticle kinetic energy. Since the magnitudes of the hoppings along the a - and b -axis are $|t_b| > |t_a|$, the repulsion is stronger along the b -axis, so that this term forces the instability to occur along the a -axis [see Fig. 5(a), and corresponding Fermi surface in Fig. 5(b)].

- Increasing the doping reduces the contribution of V_{res} to V_{tot} , causing the strongly enhanced $\chi_{pp}^0(\mathbf{q})$ along the b -axis, starting at $p \approx 0.12$, to rotate \mathbf{q}_{CDW} from the a - to the b -axis of the YBCO unit cell [see Fig. 5a]. Notably, the magnitude of \mathbf{q}_{CDW} remains constant across the transition, as the minimum of $V_{\text{tot}}(\mathbf{q})$ is only weakly dependent on the orientation of \mathbf{q} , cf. Supplementary Note 3. For the considered parameters, the Fermi surface is closed at $(\pi, 0)$ while remaining open at $(0, \pi)$ [see Fig. 5c]. Consequently, the

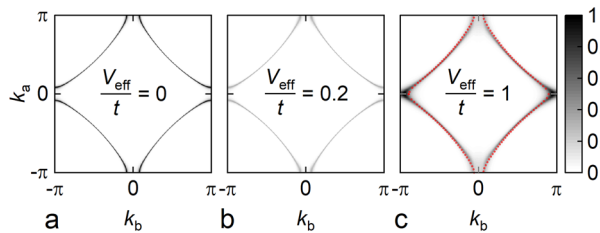


Fig. 3 | Fermi surface within the CPA for different values of effective potential V_{eff}/t . **a** $V_{\text{eff}}/t = 0$; **b** $V_{\text{eff}}/t = 0.2$; **c** $V_{\text{eff}}/t = 1$. In all cases, the concentration of one-dimensional strips is $f = 0.15$, the next-nearest neighbor hopping is $t'/t = -0.15$ and the doping is $p = 0.12$. The red dashed line corresponds to a tight-binding parametrization derived from $t_{b,a} = t(1 \pm \alpha)$ and anisotropy parameter $\alpha = 0.015$.

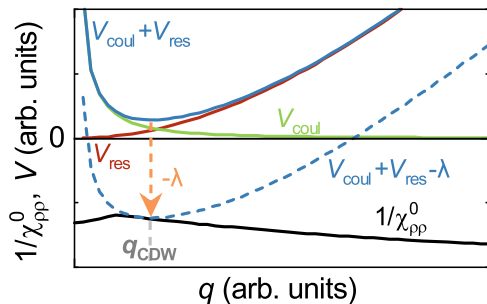


Fig. 4 | CDW instability within the frustrated phase separation scenario (sketch). The effective random-phase-approximation (RPA) expression $1/\chi_{pp}^0(q) - V_{\text{tot}}(q) = 0$ where $\chi_{pp}^0(q)$ is the charge susceptibility of the non-interacting quasiparticle system. The total interaction $V_{\text{tot}}(q)$ (blue dashed line) is given by the sum of a long-range Coulomb interaction $V_{\text{coul}}(q)$ (green line), a residual short-range repulsion between quasiparticles $V_{\text{res}}(q)$ as customary in Fermi liquid theory (red line), and an attractive interaction $V_{\text{attr}}(q)$, which for simplicity we suppose momentum independent ($V_{\text{attr}} = -\lambda$), providing the vertical shift highlighted by the orange dashed arrow. All these interactions have the symmetry of the electronic system and in the nematic state therefore acquire C_2 symmetry as discussed in the Supplementary Note 3 where in Supplementary Fig. S6 we also show an actual plot for a representative doping.

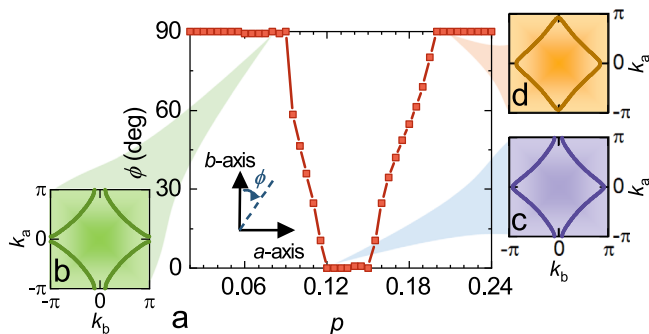


Fig. 5 | Doping dependent orientation of the CDW instability. **a** Angle (with respect to b -axis) of the CDW wave vector as a function of doping for a Holstein electron-phonon coupling $V^{\text{ph}}(q) \equiv -\lambda$. The other parameters used in the model, built in the frustrated phase separation scenario, are the following: $a/b = 0.98$, $t'/t = -0.17$, $V_{\text{coul}}/t = 0.5$, and the anisotropy parameter $\alpha = 0.015$. In the three insets, the nematic Fermi surfaces obtained using these parameters are shown as a function of doping, in case **b** $p = 0.08$, **c** $p = 0.13$ [similar to the one of Fig. 3c] and **d** $p = 0.20$. See Supplementary Note 3 for the discussion of the anisotropy of $V_{\text{coul}}(q)$ and $V_{\text{res}}(q)$ in the nematic system.

CDW modulation maintains its orientation along the b -direction in the doping range $0.12 \lesssim p \lesssim 0.15$. A strong nesting indeed occurs along the b -axis, arising from the small Fermi velocity v_{kb} around $(\pi, 0)$ and the concomitant enhanced density of states.

- At $p \approx 0.15$, the Fermi surface gets closed also at $(0, \pi)$, while still being nematic [see Fig. 5d]. Upon increasing doping from $p = 0.15$ to $p = 0.20$, its topology favors a finite angle between \mathbf{q}_{CDW} and the orthorhombic b -axis. Consequently, the instability vector \mathbf{q}_{CDW} rotates from the b - back to the a -axis, where it remains for $p \gtrsim 0.20$. In this regime, anisotropic interactions again dominate the orientation of q_{CDW} over the reduced nesting along the b -axis.

Three points regarding the validity of these results should be added: (a) We do not consider pinning effects which would turn the continuous rotation of the CDW vector again into an abrupt transition from the b - to a -axis (and vice versa); (b) The model Eq. (2) includes neither magnetism nor the effect of CDW fluctuations⁴⁵ which suppress the CDW instability at low and large doping, respectively; (c) Our treatment of correlations with $U \rightarrow \infty$ might overestimate the anisotropy of $V_{\text{tot}}(q)$, suggesting a larger doping regime for the b -axis oriented CDW for a more realistic repulsive interactions with $U/t \approx 8$. These points collectively imply that our model predicts a b -axis oriented unidirectional CDW, consistent with measurements in ref. 38, across the majority of the doping range where experimental evidence of CDW is detected in cuprates ($0.08 < p < 0.16$).

Conclusions

In summary we have developed a model that accounts for interface effects between HTS thin films and substrate. The nanostructured morphology of the substrate surface creates strong bonds between the films and the substrate, introducing an additional substrate potential that modifies the Fermi surface and induces a CDW instability. The model successfully reproduces the nematic Fermi surface and unidirectional CDW observed in the experiment³⁸. Our finding opens new prospective to tune the ground state of HTS by properly nanopatterning the substrate surface to induce a substrate potential with well-defined symmetries.

Data availability

All datasets generated and analyzed throughout this work are available from the corresponding authors upon reasonable request.

Code availability

The theoretical analysis was carried out with FORTRAN codes to implement the analysis of Eqs. (1,2) as specified in the supplemental material. Although the same task could easily be performed with other standard softwares, the FORTRAN codes we used are available from one of the corresponding authors [G.S.] on reasonable request.

Received: 21 February 2024; Accepted: 18 July 2024;
Published online: 09 August 2024

References

- Keimer, B., Kivelson, S. A., Norman, M. R., Uchida, S. & Zaanen, J. From quantum matter to high-temperature superconductivity in copper oxides. *Nature* **518**, 179 (2015).
- Fradkin, E., Kivelson, S. A. & Tranquada, J. M. Theory of intertwined orders in high temperature superconductors. *Rev. Mod. Phys.* **87**, 457 (2015).
- Proust, C. & Taillefer, L. The remarkable underlying ground states of cuprate superconductors. *Annu. Rev. Condens. Matter Phys.* **10**, 409 (2019).
- Kloss, T., Montiel, X., de Carvalho, V. S., Freire, H. & Pépin, C. Charge orders, magnetism and pairings in the cuprate superconductors. *Rep. Prog. Phys.* **79**, 084507 (2016).
- Phillips, P. W., Hussey, N. E. & Abbamonte, P. Stranger than metals. *Science* **377**, eabh4273 (2022).
- Varma, C. M. Quantum-critical fluctuations in 2D metals: strange metals and superconductivity in antiferromagnets and in cuprates. *Rep. Prog. Phys.* **79**, 082501 (2016).
- Zaanen, J. Planckian dissipation, minimal viscosity and the transport in cuprate strange metals. *SciPost Phys.* **6**, 061 (2019).

8. Ayres, J., Berben, M. Čulo, M. et al. Incoherent transport across the strange-metal regime of overdoped cuprates. *Nature* **595**, 661 (2021).
9. Hartnoll, S. A. & Mackenzie, A. P. Planckian dissipation in metals. *Rev. Mod. Phys.* **94**, 041002 (2022).
10. Mirarchi, G., Seibold, G., Di Castro, C., Grilli, M. & Caprara, S. The Strange-Metal Behavior of Cuprates. *Condensed Matter* **7**, 29 (2022).
11. Huang, E. W., Sheppard, R., Moritz, B. & Devereaux, T. P. Strange metallicity in the doped Hubbard model. *Science* **366**, 987 (2019).
12. Wú, W., Wang, X. & Tremblay, A. M. Non-Fermi liquid phase and linear-in-temperature scattering rate in overdoped two-dimensional Hubbard model. *Proc. Natl. Acad. Sci.* **119**, e2115819119 (2022).
13. Cha, P., Wentzell, N., Parcollet, O., Georges, A. & Kim, E. A. Linear resistivity and Sachdev-Ye-Kitaev (SYK) spin liquid behavior in a quantum critical metal with spin-1/2 fermions. *Proc. Natl. Acad. Sci.* **117**, 18341 (2020).
14. Dumitrescu, P. T., Wentzell, N., Georges, A. & Parcollet, O. Planckian metal at a doping-induced quantum critical point. *Phys. Rev. B* **105**, L180404 (2022).
15. Christos, M., Luo, Z.-X., Shackleton, H., Scheurer, M. & Sachdev, S. A model of d-wave superconductivity, antiferromagnetism, and charge order on the square lattice. *Proc. Natl. Acad. Sci.* **120**, e2302701120 (2023).
16. Patel, A. A., Guo, H., Esterlis, I. & Sachdev, S. Universal theory of strange metals from spatially random interactions. *Science* **381**, 790 (2023).
17. Arpaia, R. et al. Dynamical charge density fluctuations pervading the phase diagram of a Cu-based high-T_c superconductor. *Science* **365**, 906 (2019).
18. Arpaia, R. et al. Signature of quantum criticality in cuprates by charge density fluctuations. *Nat. Commun.* **14**, 7198 (2023).
19. Seibold, G. et al. Strange metal behaviour from charge density fluctuations in cuprates. *Commun. Phys.* **4**, 7 (2021).
20. Caprara, S., Di Castro, C., Mirarchi, G., Seibold, G. & Grilli, M. Dissipation-driven strange metal behavior. *Commun. Phys.* **5**, 2399 (2022).
21. Balm, F. et al. T-linear resistivity, optical conductivity and Planckian transport for a holographic local quantum critical metal in a periodic potential. *Phys. Rev. B* **108**, 125145 (2023).
22. Baggioli, M. & Goutéraux, B. Hydrodynamics and holography of charge density wave phases. *Rev. Mod. Phys.* **95**, 011001 (2023).
23. Mito, M. et al. Uniaxial strain effects on the superconducting transition in Re-doped Hg-1223 cuprate superconductors. *Phys. Rev. B* **95**, 064503 (2017).
24. Kim, H.-H. et al. Uniaxial pressure control of competing orders in a high-temperature superconductor. *Science* **362**, 1040 (2018).
25. Kim, H.-H. et al. Charge density waves in YBa₂Cu₃O_{6.67} probed by resonant x-ray scattering under uniaxial compression. *Phys. Rev. Lett.* **126**, 037002 (2021).
26. Boyle, T. J. et al. Large response of charge stripes to uniaxial stress in La_{1.475}Nd_{0.4}Sr_{0.125}CuO₄. *Phys. Rev. Research* **3**, L022004 (2021).
27. Choi, J. et al. Unveiling unequivocal charge stripe order in a prototypical cuprate superconductor. *Phys. Rev. Lett.* **128**, 207002 (2022).
28. Barber, M. E. et al. Dependence of T_c of YBa₂Cu₃O_{6.67} on in-plane uniaxial stress. *Phys. Rev. B* **106**, 184516 (2022).
29. Nakata, S. et al. Normal-state charge transport in YBa₂Cu₃O_{6.67} under uniaxial stress. *npj Quantum Materials* **7**, 118 (2022).
30. Guguchia, Z. et al. Designing the stripe-ordered cuprate phase diagram through uniaxial-stress, arXiv:2302.07015 (2023).
31. Gupta, N. K. et al. Tuning charge density wave order and structure via uniaxial stress in a stripe-ordered cuprate superconductor. *Phys. Rev. B* **108**, L121113 (2023).
32. Tranquada, J. M., Sternlieb, B., Axe, J., Nakamura, Y. & Uchida, S. Evidence for stripe correlations of spins and holes in copper oxide superconductors. *Nature* **375**, 561 (1995).
33. Abbamonte, P. et al. Spatially modulated 'Mottness' in La_{2-x}Ba_xCuO₄. *Nat. Phys.* **1**, 155 (2005).
34. Ghiringhelli, G. et al. Long-Range Incommensurate Charge Fluctuations in (Y,Nd)Ba₂Cu₃O_{6+x}. *Science* **337**, 821 (2012).
35. Chang, J. et al. Direct observation of competition between superconductivity and charge density wave order in YBa₂Cu₃O_{6.67}. *Nat. Phys.* **8**, 871 (2012).
36. Comin, R. & Damascelli, A. Resonant x-ray scattering studies of charge order in cuprates. *Annu. Rev. Condens. Matter Phys.* **7**, 369 (2016).
37. Arpaia, R. & Ghiringhelli, G. Charge Order at High Temperature in Cuprate Superconductors. *J. Phys. Soc. Japan* **90**, 111005 (2021).
38. Wahlberg, E. et al. Restored strange metal phase through suppression of charge density waves in underdoped YBa₂Cu₃O_{7-δ}. *Science* **373**, 1506 (2021).
39. Arpaia, R., Andersson, E., Trabaldo, E., Bauch, T. & Lombardi, F. Probing the phase diagram of cuprates with YBa₂Cu₃O_{7-δ} thin films and nanowires. *Phys. Rev. Mat.* **2**, 024804 (2018).
40. Arpaia, R. et al. Untwinned YBa₂Cu₃O_{7-δ} thin films on MgO substrates: A platform to study strain effects on the local orders in cuprates. *Phys. Rev. Mat.* **3**, 114804 (2019).
41. Emery, V. J. & Kivelson, S. A. Frustrated electronic phase separation and high-temperature superconductors. *Physica C* **209**, 597 (1993).
42. Raimondi, R., Castellani, C., Grilli, M., Bang, Y. & Kotliar, G. Charge collective modes and dynamic pairing in the three-band Hubbard model. II. Strong-coupling limit. *Phys. Rev. B* **47**, 3331 (1993).
43. Castellani, C., Di Castro, C. & Grilli, M. Singular Quasiparticle Scattering in the Proximity of Charge Instabilities. *Phys. Rev. Lett.* **75**, 4650 (1995).
44. Becca, F., Tarquini, M., Grilli, M. & Di Castro, C. Charge-density waves and superconductivity as an alternative to phase separation in the infinite-U Hubbard-Holstein model. *Phys. Rev. B* **54**, 12443 (1996).
45. Andergassen, S., Caprara, S., Di Castro, C. & Grilli, M. Anomalous Isotopic Effect Near the Charge-Ordering Quantum Criticality. *Phys. Rev. Lett.* **87**, 056401 (2001).
46. Seibold, G. et al. Spectral properties of incommensurate charge-density wave systems. *Eur. Phys. J. B* **13**, 87 (2000).
47. Caprara, S., Di Castro, C., Seibold, G. & Grilli, M. Dynamical charge density waves rule the phase diagram of cuprates. *Phys. Rev. B* **95**, 224511 (2017).

Acknowledgements

We acknowledge support by the Swedish Research Council (VR), under the Projects 2018-04658 (F.L.), 2020-04945 (R.A.) and 2020-05184 (T.B.), by the University of Rome Sapienza, under the projects Ateneo 2021 (RM12117A4A7FD11B), Ateneo 2022 (RM12218162CF9D05), Ateneo 2023 (RM123188E830D258) (G.M., C.D.C., M.G., S.C.), by the Italian Ministero dell'Università e della Ricerca, under the PNRR MUR project PE0000023-NQSTI (M.G., S.C.), by the Deutsche Forschungsgemeinschaft, under SE 806/20-1 (G.S.).

Author contributions

E.W. and R.A. grew the samples; E.W. performed the transport measurements; A. K., R.A., E.W. performed the AFM measurements; F.L., R.A., A. K. and T.B. interpreted the AFM measurements with the theoretical insights of M. G., S. C., C.D.C. and G. S.; G. M. and G. S. performed the theoretical calculations and M. G., S. C. and C. D. C. contributed to the theoretical analysis of the theoretical data. F. L., R. A., and G. S. wrote the paper and all authors contributed to the discussion of the paper.

Funding

Open access funding provided by Chalmers University of Technology.

Competing interests

The authors declare no competing interests.

Additional information

Supplementary information The online version contains supplementary material available at <https://doi.org/10.1038/s43246-024-00582-5>.

Correspondence and requests for materials should be addressed to Floriana Lombardi or Götz Seibold.

Peer review information *Communications Materials* thanks the anonymous reviewers for their contribution to the peer review of this work. Primary Handling Editor: Aldo Isidori.

Reprints and permissions information is available at <http://www.nature.com/reprints>

Publisher's note Springer Nature remains neutral with regard to jurisdictional claims in published maps and institutional affiliations.

Open Access This article is licensed under a Creative Commons Attribution 4.0 International License, which permits use, sharing, adaptation, distribution and reproduction in any medium or format, as long as you give appropriate credit to the original author(s) and the source, provide a link to the Creative Commons licence, and indicate if changes were made. The images or other third party material in this article are included in the article's Creative Commons licence, unless indicated otherwise in a credit line to the material. If material is not included in the article's Creative Commons licence and your intended use is not permitted by statutory regulation or exceeds the permitted use, you will need to obtain permission directly from the copyright holder. To view a copy of this licence, visit <http://creativecommons.org/licenses/by/4.0/>.

© The Author(s) 2024